

EGMSpy: an open-source Python toolkit for scalable data handling, classification, clustering, and visualisation of Copernicus EGMS InSAR data

F. Catani^{*1}, C. Palmieri¹, R. Todde¹, L. Nava^{2, 3}, and M. Floris¹

¹Department of Geosciences – MISSLab (Machine Intelligence and Slope Stability Lab),
University of Padova, Padova, Italy

²Department of Geography, King's College London, London, United Kingdom

³King's Institute for Artificial Intelligence, King's College London, London, United Kingdom

May 2026

*This is a non-peer-reviewed preprint posted on **EarthArXiv** (<https://eartharxiv.org>).*

DOI: [10.31223/X55B59](https://doi.org/10.31223/X55B59)

Abstract

The Copernicus European Ground Motion Service (EGMS) provides millimetre-accuracy line-of-sight displacement measurements for over five billion coherent scatterers across Europe, derived from Sentinel-1 SAR interferometry over the period 2015–2023. Despite the unprecedented spatial coverage and measurement density of this dataset, no open-source integrated toolchain exists for processing, classifying, clustering, and interactively visualising EGMS data at the regional to continental scale without resorting to subsampling or proprietary software. In this paper, we introduce **EGMSpy**, a fully open-source Python pipeline that ingests raw EGMS L2b CSV tiles, compresses them into a federated split-GeoParquet database (metadata and time series stored separately, linked by a unique point identifier), applies a physics-informed hybrid rule/GMM time series classifier to assign each point to a geophysical deformation class, groups spatially and dynamically coherent deforming areas using a velocity-weighted three-dimensional DBSCAN algorithm, and serves the entire dataset to an interactive Leaflet.js web viewer via a Flask/DuckDB REST bridge capable of sub-100 ms viewport queries over hundreds of millions of points. The pipeline is demonstrated on the northern Italy EGMS L2b dataset (2019–2023), comprising 433 tile pairs (≈ 300 million coherent scatterers, 104 GB on disk), processed on a single workstation. Internal quality control confirms that the toolkit's OLS-derived velocity features are consistent with the official EGMS pre-computed velocities (RMSE = 0.096 mm yr⁻¹, bias = -0.001 mm yr⁻¹, $r = 0.9993$, $n = 99,751$). All code is released under the MIT

*Corresponding author: filippo.catani@unipd.it

licence and is available at <https://github.com/fcatani/EGMSpy> (repository in beta v1.0).

Keywords: InSAR; EGMS; GeoParquet; DuckDB; time series classification; DBSCAN; geohazard; subsidence

1 Introduction

1.1 The EGMS dataset and its challenges at scale

Satellite SAR interferometry (InSAR) is widely recognised as one of the primary tools for monitoring ground deformation at the regional scale, with millimetre-level accuracy in the detection of surface displacements associated with landslides, ground subsidence, volcanic activity, seismic deformation, and structural instability (Ferretti et al., 2001; Berardino et al., 2002; Catani et al., 2005; Hooper et al., 2012). The Copernicus *European Ground Motion Service* (EGMS; Crosetto et al. 2020; Costantini et al. 2017) represents the most ambitious application of InSAR to date, providing GNSS-calibrated line-of-sight (LOS) displacement time series for over five billion coherent scatterers across all Copernicus Participating States at an average spatial density of ≈ 1 point per 20 m spacing ($\approx 400 \text{ m}^2$) in urban areas.

Despite its extraordinary coverage, the operational use of EGMS data presents several challenges. (i) A single national coverage may contain 10^8 – 10^9 points. The CSV format distributed by the portal is poorly suited to large-scale analytical queries; a single tile can exceed 2 GB. (ii) Different orbital tracks have different acquisition schedules, producing CSV files with different sets of date columns. Federating these into a single queryable database requires schema-aware handling. (iii) Each point’s time series may exhibit linear trends, acceleration, seasonal signals, abrupt jumps, or noise-dominated behaviour. No automated, physics-informed classifier exists for the EGMS product. (iv) Identifying spatially coherent groups of deforming points (e.g. a landslide body, a subsiding building) requires clustering in a joint spatial–velocity space, not simple 2D spatial grouping. (v) The EGMS portal viewer is limited to pre-defined spatial extents and does not support classification-based colour coding or multi-point time series overlay. Standard GIS tools (QGIS, ArcGIS) struggle with tens of millions of points.

1.2 Existing tools and their limitations

Several open-source InSAR processing packages exist for generating displacement time series from raw SAR data: MintPy (Yunjun et al., 2019), StaMPS (Hooper, 2008), ESA SNAP, and GAMMA (Werner et al., 2000). However, these tools operate *upstream* of the EGMS product — they produce displacement time series from raw Sentinel-1 SLC data, which requires significant computational resources and expertise.

For users who wish to *analyse* the already-processed EGMS product downstream, no equivalent open-source toolchain exists. The EGMS Explorer portal provides a web viewer and individual tile downloads, but offers no programmatic API, no time series classification, no clustering, and no ability to handle multi-tile datasets as a single queryable

74 database. EGMStoolkit (Hrysiewicz et al., 2024) provides automated download function-
75 ality but does not address storage, classification, or visualisation.

76 1.3 Scope and contributions of this work

77 This paper presents **EGMSpy**, a Python pipeline that addresses the five challenges out-
78 lined above. The specific contributions are:

- 79 1. A **split-GeoParquet storage architecture** with DuckDB federation that reduces
80 CSV storage by $\approx 70\%$ and enables sub-100 ms analytical queries over 10^8 points on
81 a single workstation.
- 82 2. A **physics-informed hybrid time series classifier** assigning each EGMS point
83 to one of seven geophysical classes (stable, noisy, linear, accelerating, decelerat-
84 ing, variable, other) plus four boolean descriptor flags (periodic, jumpy, variable,
85 noisy_trend), using an 18-feature vectorised extraction pipeline followed by a rule-
86 primary / GMM-secondary decision architecture.
- 87 3. A **velocity-weighted 3D DBSCAN clustering algorithm** that simultaneously
88 enforces spatial proximity and velocity similarity, producing geophysically meaning-
89 ful deformation clusters with convex-hull polygon outputs.
- 90 4. A **two-level sub-clustering** step that stratifies parent clusters by time series class,
91 enabling differentiation of spatially co-located but behaviourally distinct deforma-
92 tion phenomena.
- 93 5. An **interactive web viewer** capable of rendering up to 200,000 filtered and clas-
94 sified InSAR points in a single Canvas 2D pass, with adaptive zoom-level spatial
95 thinning, time series pop-up plots, and cluster polygon overlays.
- 96 6. A **PyQt6 GUI** orchestrating the full pipeline, making the toolkit accessible without
97 command-line expertise.

98 2 Data

99 2.1 EGMS L2b product

100 The EGMS Level 2b product (Copernicus Land Monitoring Service, 2022) contains GNSS-
101 calibrated LOS displacement time series derived from Sentinel-1 IW mode SAR data
102 processed with the Persistent Scatterer InSAR (PSI) and Small Baseline Subset (SBAS)
103 techniques. Each measurement point is characterised by 24 metadata attributes (Ta-
104 ble 1) including mean LOS velocity, temporal coherence, orbital geometry, and LOS
105 unit vector components, followed by $N_t \approx 200\text{--}300$ displacement observations (mm)
106 at dates spanning the 2015–2023 period (2019–2023 for the current release used here).
107 Data are freely accessible via the Copernicus Land Monitoring Service portal (<https://egms.land.copernicus.eu/>)
108 subject to the Copernicus Data Policy.

109 2.2 Demonstration area: Northern Italy

110 We demonstrate the EGMSpy pipeline on a test area that covers northern Italy, including
111 the Po River Basin and surrounding pre-Alpine and Alpine foothills, bounded approxi-
112 mately by $6.55^\circ\text{E}\text{--}14.02^\circ\text{E}$, $43.63^\circ\text{N}\text{--}47.18^\circ\text{N}$ (Fig. 2). This region is characterised by a

113 wide variety of deformation phenomena: widespread agricultural and urban subsidence in
114 the Po plain and delta (Colesanti et al., 2003; Raspini et al., 2019), active landsliding on
115 Alpine and Apennine slopes (Casagli et al., 2017), and seasonal signals associated with
116 groundwater fluctuations and frost-heave, global warming-related processes in mountain
117 areas.

118 The dataset comprises 433 tile pairs processed from 517 originally downloaded tiles (84
119 tiles were excluded due to zero valid measurements, typically covering sea or other low-
120 backscatter areas). The total point count is approximately **300 million coherent scat-**
121 **terers** across 11 Sentinel-1 orbital tracks (ascending tracks 015, 022, 044, 066, 088, 095,
122 117, 139; descending tracks 146, 161, 168). The raw data occupy approximately 180 GB
123 as EGMS ZIP archives; after conversion to split uncompressed GeoParquet the processed
124 dataset occupies 104 GB (22.8 GB metadata, 81.6 GB time series).

125 **3 Design and Implementation**

126 **3.1 Overview and pipeline architecture**

127 The EGMSpy pipeline consists of nine sequential processing steps (Fig. 1), each imple-
128 mented as an independent Python script callable from both the command line and the
129 PyQt6 GUI. All processing steps are non-destructive: each step only *adds* columns to
130 the metadata Parquet files; the time series Parquet files are never modified after the ini-
131 tial conversion and their information content remains consistent with the original EGMS
132 product, unless data gaps are corrected.

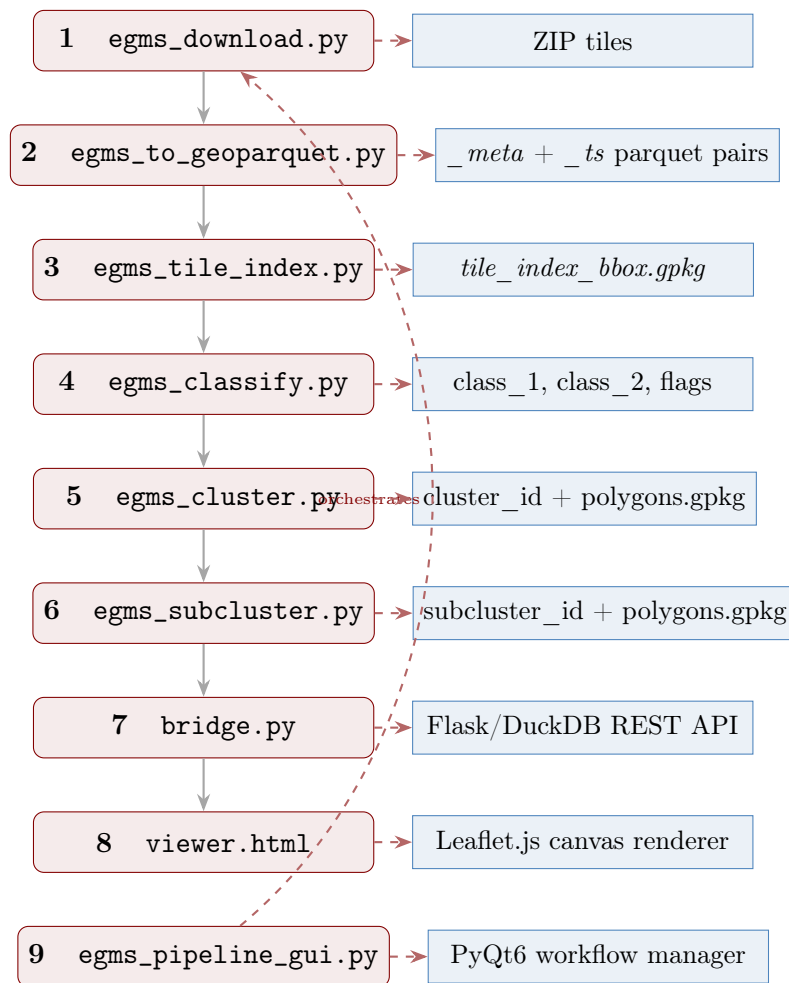


Figure 1: Full processing pipeline. Each step adds new columns to the `_meta.parquet` files (classification labels, cluster IDs) while the `_ts.parquet` files remain unchanged after conversion. The PyQt6 GUI (step 9) orchestrates all steps as monitored subprocesses.

133 3.2 Storage: split GeoParquet and DuckDB federation

134 Storage is one of the critical bottlenecks in big-data analysis, and InSAR is not an excep-
 135 tion when the datasets cover regions or countries at a density such as the one provided
 136 by the EGMS service.

137 In EGMSpy, storage efficiency is increased by converting each input CSV tile into two
 138 coupled Parquet files: (i) the `<stem>_meta.parquet` file — where the 24 EGMS meta-
 139 data columns plus derived columns (orbit, max_gap_days, n_acquisitions) and WGS84
 140 geometry are stored in GeoParquet 1.0, EPSG:4326 format with Snappy compression; and
 141 (ii) the `<stem>_ts.parquet` file — where the time series with pid plus one float32 column
 142 per acquisition date (200–300 columns) is permanently memorised.

143 Files within a pair `meta/ts` are linked by the unique point identifier pid. All metadata
 144 files across all tiles are federated into a single DuckDB virtual view at query time:

```

145 CREATE VIEW all_metadata AS
146 SELECT * FROM read_parquet('processed/**/*_meta.parquet',
147
```

148

union_by_name=True)

Table 1: EGMS L2b metadata columns (24 fixed) common to every tile, as defined in the EGMS product specification ([Copernicus Land Monitoring Service, 2022](#)).

#	Column	Description
1	pid	Unique point identifier (alphanumeric string)
2	mp_type	Measurement point type (0 = PS, 1 = DS)
3	latitude	WGS84 latitude ($^{\circ}$, float64)
4	longitude	WGS84 longitude ($^{\circ}$, float64)
5	easting	LAEA EPSG:3035 easting (m, float32)
6	northing	LAEA EPSG:3035 northing (m, float32)
7	height	Ellipsoidal height above LAEA datum (m)
8	height_wgs84	Ellipsoidal height above WGS84 ellipsoid (m)
9	line	SAR image line index (integer)
10	pixel	SAR image pixel index (integer)
11	rmse	Deformation model RMSE (mm)
12	temporal_coherence	Temporal coherence [0–1]
13	amplitude_dispersion	Amplitude dispersion index
14	incidence_angle	Satellite incidence angle ($^{\circ}$)
15	track_angle	Satellite track heading angle ($^{\circ}$)
16	los_east	LOS unit vector, east component
17	los_north	LOS unit vector, north component
18	los_up	LOS unit vector, vertical component
19	mean_velocity	Mean LOS velocity (mm yr^{-1})
20	mean_velocity_std	Mean velocity standard deviation (mm yr^{-1})
21	acceleration	LOS acceleration (mm yr^{-2})
22	acceleration_std	Acceleration standard deviation (mm yr^{-2})
23	seasonality	Seasonal amplitude (mm)
24	seasonality_std	Seasonal amplitude standard deviation (mm)

150 The `union_by_name=True` flag handles schema heterogeneity between orbital tracks (dif-
 151 ferent acquisition date columns per track). Metadata columns are stored as float32 (ex-
 152 cept WGS84 coordinates retained at float64), achieving approximately 70% file size re-
 153 duction relative to the original CSV. All spatial computations (DBSCAN, convex hulls)
 154 use EPSG:3035 (LAEA Europe) for equal-area distance preservation ([Copernicus Land
 155 Monitoring Service, 2022](#)), while geometry storage and web display use EPSG:4326.

156 3.3 Spatial tile index

157 After conversion, a spatial QC index is built from all metadata files by `egms_tile_index.py`
 158 (Fig. 2).

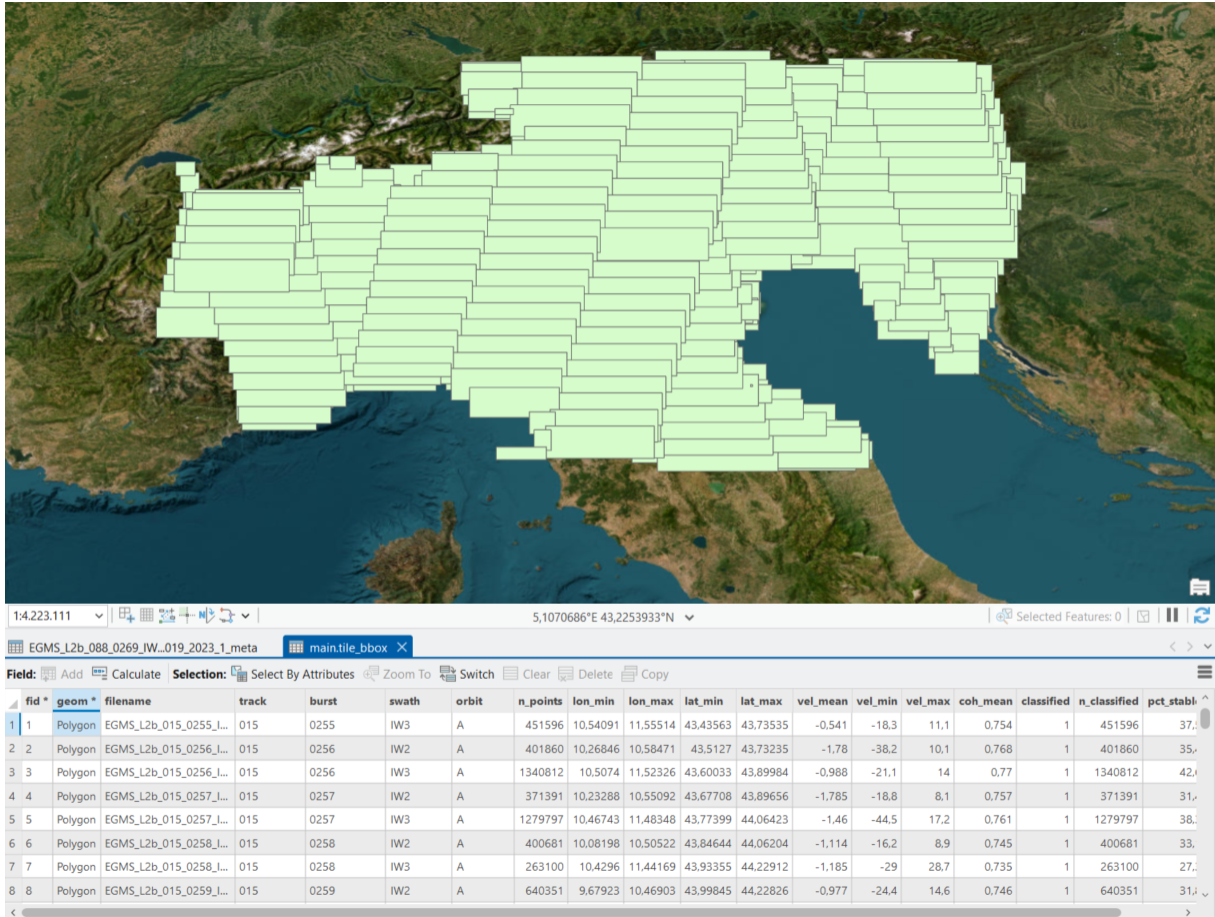


Figure 2: Spatial tile index for the northern Italy demonstrator area, visualised in ArcGIS. Each polygon represents the bounding box of one EGMS L2b tile (433 valid tiles shown). The attribute table (lower panel) records, for each tile: track, burst, swath, orbit direction, point count (`n_points`), geographic extent, mean/min/max velocity, mean coherence, and classification status (`classified`, `n_classified`). Tiles covering open sea and high-Alpine terrain above the vegetation/infrastructure line contain few or no coherent scatterers and appear as sparse or empty tiles in the index. The full dataset covers approximately 6.5°E – 14.0°E , 43.6°N – 47.2°N , spanning the Po Plain, pre-Alpine foothills, Alpine chain, and northern Apennines.

159 For each tile, the script reads only the columns needed (`pid`, `longitude`, `latitude`,
 160 `mean_velocity`, `temporal_coherence`, `orbit`, `class_1` if present), computes the axis-
 161 aligned bounding box $[\lambda_{\min}, \phi_{\min}, \lambda_{\max}, \phi_{\max}]$, and reports classification coverage (% of
 162 rows with non-null `class_1`). In the demonstrator, processing is parallelised with `joblib`
 163 (threading backend); all 433 tiles are indexed in ≈ 5 min at $1.55 \text{ files s}^{-1}$ using 16 workers.
 164 The output GeoPackage (`tile_index_bbox.gpkg`, EPSG:4326) is directly loadable in
 165 QGIS and enables immediate visual QC of coverage and classification completeness by
 166 styling on the `classified` attribute.

167 3.4 Winter-gap correction

168 SAR acquisitions over Alpine and high-elevation terrain are frequently suspended during
169 winter months (predominantly November–March) due to snow cover causing temporal
170 decorrelation and loss of coherent scatterers. These gaps produce stretches of null val-
171 ues in the `_ts.parquet` time series that, if left untreated, bias the OLS slope and har-
172 monic fits in `egms_classify.py` by distorting the effective time baseline. The additional
173 EGMSpy module `egms_correct.py` detects contiguous null runs exceeding a configurable
174 minimum duration (default: 30 days) and fills them with gap-preserving linear interpo-
175 lation between the last valid value before and the first valid value after each gap. The
176 interpolated values are flagged and excluded from jump detection; the maximum gap
177 duration (`max_gap_days`) is recorded as a derived metadata column and can be used
178 as a data-quality filter in downstream queries. The quality check result in Section 4.1
179 confirms that this procedure introduces no detectable bias in the OLS velocity (residual
180 bias = $-0.001 \text{ mm yr}^{-1}$).

181 3.5 Time series classification

182 3.5.1 Overview and design strategy

183 At national and continental scales, InSAR ground deformation heuristic interpretation
184 might be rendered impossible by the sheer amount of data available, if not supported by
185 automation. Early approaches relied on hand-crafted statistical features combined with
186 rule-based or supervised classifiers to distinguish stable, linear, and non-linear trend pat-
187 terns (Berti et al., 2013; Cigna et al., 2011; Mirmazloumi et al., 2022). More recent work
188 has moved toward deep learning architectures, including CNN–LSTM models that jointly
189 exploit temporal deformation patterns and spatial morphological context to classify the
190 entire deformation areas into geophysical process types such as landslides, subsidence,
191 mining, or deep-seated gravitational deformations (Dong et al., 2025). However, process-
192 level classification of spatially aggregated objects requires that individual measurement
193 points have already been assigned kinematic labels — a per-point characterisation that
194 existing frameworks do not provide at the scale of continental InSAR products such as
195 EGMS. EGMSpy addresses this gap through a physics-informed hybrid rule/GMM classi-
196 fier that assigns each of the $\approx 283 \text{ M}$ northern Italy PS points to one of seven geophysical
197 classes, operating directly on the per-point displacement time series without requiring
198 spatial aggregation or auxiliary geomorphological data. Specifically, `egms_classify.py`
199 implements a **hybrid rule-primary / GMM-secondary** classifier (v3 scheme). The
200 key design principle is that physics-based rule labels are *final and cannot be overridden*:
201 the Gaussian Mixture Model (GMM) is applied only to genuinely ambiguous residual
202 points (those unresolved by all rules). This architecture prevents the minority-class col-
203 lapse observed in pure GMM approaches, where classes such as *noisy* and *variable* are
204 absorbed into the dominant *stable* class when GMM components are initialised without
205 physics-based constraints.

206 3.5.2 Classification scheme

207 The classification of displacement time series into physically interpretable deformation cat-
208 egories is a prerequisite for operational geohazard analysis at all scales. Different surface

209 processes — including ground subsidence, accelerating slope failures, seasonally driven
 210 creep, and abrupt infrastructure displacements — produce kinematically distinct time se-
 211 ries signatures that, if left undifferentiated, cannot be exploited for early warning or risk
 212 mitigation (Casagli et al., 2023; Berti et al., 2013; Cigna et al., 2011). Translating raw
 213 velocity fields into labelled deformation classes (and clusters) enables the triage of hazard-
 214 relevant signals from the dominant background of stable or noise-dominated scatterers,
 215 directly supporting the prioritisation of field inspections and the calibration of physically
 216 based failure-forecasting models (Casagli et al., 2023; Mirmazloumi et al., 2022; Catani
 217 et al., 2005). Seven primary classes and four boolean descriptor flags are defined here,
 218 drawing on classification schemes proposed across multiple natural and anthropogenic
 219 hazard contexts — including slow-moving landslides, urban subsidence, mining deforma-
 220 tion, and seasonal groundwater cycling (Berti et al., 2013; Cigna et al., 2011; Mirmazloumi
 221 et al., 2022; Dong et al., 2025) — so that the taxonomy covers the full kinematic diversity
 222 observable in a continental-scale product such as EGMS without imposing process-specific
 223 assumptions at the classification stage (Table 2).

Table 2: Time series classification scheme (v3). Primary classes are mutually exclusive; descriptor flags are independent and may co-occur with any primary class.

Code	Class	Criterion
0	stable	$ v < v_s$, RMSE after linear detrend $\leq \sigma_n$
1	noisy	$ v < v_s$, RMSE after linear detrend $> \sigma_n$
2	linear	$ v \geq v_s$, sustained trend ($R_{\text{lin}}^2 \geq 0.65$)
3	accel	Accelerating deformation (sign-consistent v_{diff} and quadratic improvement)
4	decel	Decelerating deformation
5	variable	$ v < v_s$, erratic signal (high CUSUM, low R^2)
6	other	Ambiguous residual, resolved by GMM
Descriptor flag		Criterion
periodic		Seasonal harmonic significant: $R_{\text{seas}}^2 - R_{\text{lin}}^2 > 0.15$
jumpy		≥ 1 non-seasonal step $\geq j_{\text{min}}$ mm in deseasonalised residuals
variable_flag		High CUSUM changepoint score (erratic rate changes)
noisy_trend		Moving point ($ v \geq v_s$) with high scatter after full detrend and deseasoning

224 3.5.3 Feature extraction

225 For each point, 18 scalar features are extracted from the LOS displacement time series
 226 $\{d_1, \dots, d_{N_t}\}$ (mm) at times $\{t_1, \dots, t_{N_t}\}$ (fractional years). The feature set draws on pa-
 227 rameterisations established in the InSAR time series classification literature (Berti et al.,
 228 2013; Cigna et al., 2011; Mirmazloumi et al., 2022), extended here with a harmonic de-
 229 composition (Chen et al., 2026) and a CUSUM-based changepoint score (Ghaderpour
 230 et al., 2024) to capture seasonal signals and rate instability respectively. All computa-
 231 tions are vectorised over the full $M \times N_t$ chunk array using batch NumPy Ordinary Least
 232 Squares via `einsum`, avoiding any Python loop over points (Table 3). The choice of OLS
 233 unweighted estimator over a more rigorous one such as Theil-Shen, is justified by the com-
 234 putational constraint of processing 10^8 – 10^9 points, and by the demonstrated consistency

235 of OLS estimations with the official EGMS velocities (see Section 4.1).

236 **Linear model.** The design matrix for a centred linear fit is:

$$\mathbf{L} = \begin{pmatrix} 1 & t_1 - \bar{t} \\ \vdots & \vdots \\ 1 & t_{N_t} - \bar{t} \end{pmatrix} \quad (1)$$

237 The OLS solution $\hat{\boldsymbol{\beta}} = (\mathbf{L}^\top \mathbf{L})^{-1} \mathbf{L}^\top \mathbf{d}$ yields the mean velocity $v = \hat{\beta}_1$ (mm yr⁻¹) and the
238 coefficient of determination:

$$R_{\text{lin}}^2 = 1 - \frac{\|\mathbf{d} - \mathbf{L}\hat{\boldsymbol{\beta}}\|^2}{\|\mathbf{d} - \bar{d}\|^2} \quad (2)$$

239 **Split-half velocities.** Separate OLS slopes are fitted to the first and second halves of
240 the time span ($I_1 = \{i : i < N_t/2\}$, $I_2 = \{i : i \geq N_t/2\}$), giving v_1 and v_2 . Their
241 difference:

$$v_{\text{diff}} = v_2 - v_1 \quad (\text{mm yr}^{-1}) \quad (3)$$

242 is the primary indicator of acceleration or deceleration.

243 **Harmonic (seasonal) fit.** Annual and semi-annual harmonics are fitted jointly with
244 the linear trend:

$$\mathbf{H} = \begin{pmatrix} 1 & \tau_1 & \cos 2\pi\tau_1 & \sin 2\pi\tau_1 & \cos 4\pi\tau_1 & \sin 4\pi\tau_1 \\ \vdots & \vdots & \vdots & \vdots & \vdots & \vdots \end{pmatrix} \quad (4)$$

245 where $\tau = t - \bar{t}$. The **periodic** flag is set when the R^2 improvement over the linear-only
246 fit exceeds 0.15.

247 **Quadratic fit.** The quadratic coefficient $\hat{\gamma}_2$ (mm yr⁻²) from fitting $\mathbf{Q} = [1, \tau, \tau^2]$ quan-
248 tifies the rate of velocity change. Its R^2 improvement over the linear fit, q_{R^2} , is used
249 jointly with v_{diff} to detect acceleration and deceleration.

250 **Jump detection.** First differences of the deseasonalised residuals $r_i = d_i - \hat{d}_i^{(\text{harm})}$ are
251 examined for abrupt steps:

$$\delta_i = r_i - r_{i-1} \quad (5)$$

252 The **jumpy** flag is set when ≥ 1 step satisfies $|\delta_i| \geq j_{\text{min}}$ outside the seasonal envelope.

CUSUM changepoint score.

$$S_k = \sum_{i=1}^k (r_i - \bar{r}), \quad \text{cusum_score} = \frac{\max_k S_k - \min_k S_k}{\sigma_r \sqrt{N_t}} \quad (6)$$

253 A high CUSUM score indicates an erratic or non-stationary deformation signal and drives
254 the `variable_flag`.

Table 3: Complete 18-feature vector extracted per InSAR point.

Idx	Name	Description
0	v_robust	OLS slope: mean LOS velocity (mm yr^{-1})
1	v_first_half	Mean velocity, first 50% of time span
2	v_second_half	Mean velocity, second 50% of time span
3	v_diff	$v_2 - v_1$ (mm yr^{-1})
4	rmse_detrended	RMSE after linear detrend (mm)
5	rmse_deseason	RMSE after detrend + harmonic removal (mm)
6	seasonal_amp	Annual harmonic amplitude (mm)
7	seasonal_r2	R^2 of harmonic fit on detrended series
8	quad_coeff	Quadratic coefficient (mm yr^{-2})
9	quad_r2	R^2 improvement: quadratic over linear
10	n_jumps_nonseas	Count of non-seasonal steps $\geq j_{\min}$
11	jump_max_mm	Largest step magnitude (mm)
12	n_valid_frac	Fraction of non-null acquisitions
13	acf_lag1	Lag-1 autocorrelation of detrended residuals
14	cusum_score	CUSUM changepoint score (normalised)
15	velocity_r2	R^2 of linear fit
16	range_mm	Total range $\max(d) - \min(d)$ (mm)
17	noise_p90	90th percentile of $ \delta_i $

255 3.5.4 Rule-based classification

256 Rules are evaluated in strict priority order on the standardised feature vector of each
257 point; the first matching condition assigns the final label and evaluation halts. Default
258 parameters for the North Italy demonstrator dataset are: $v_s = 2.5 \text{ mm yr}^{-1}$, $\sigma_n = 3.0 \text{ mm}$,
259 $\theta_q = 0.15$, $c_{\text{thresh}} = 1.5$.

Algorithm 1 Rule-primary classifier (applied independently per point)

Require: feature vector $(v, \text{rmse_dt}, \text{cusum}, R_{\text{lin}}^2, q_{R^2}, v_{\text{diff}}, \hat{\gamma}_2)$; thresholds $v_s, \sigma_n, \theta_q, c_{\text{thresh}}$

Ensure: class label $\ell \in \{0, 1, 2, 3, 4, 5, 6\}$

```

1: if  $|v| < v_s$  then
2:   if  $\text{rmse\_dt} \leq \sigma_n$  then
3:     return  $\ell = 0$  (stable)
4:   else if  $\text{cusum} > c_{\text{thresh}}$  and  $R_{\text{lin}}^2 < 0.5$  then
5:     return  $\ell = 5$  (variable)
6:   else
7:     return  $\ell = 1$  (noisy)
8:   end if
9: else  $\triangleright |v| \geq v_s$ : moving point
10:  if  $q_{R^2} > \theta_q$  and  $R_{\text{lin}}^2 < 0.85$  then
11:    if  $\text{sgn}(v_{\text{diff}}) = \text{sgn}(v)$  and  $\hat{\gamma}_2 \cdot v < 0$  then
12:      return  $\ell = 3$  (accel)
13:    else if  $\text{sgn}(v_{\text{diff}}) \neq \text{sgn}(v)$  and  $\hat{\gamma}_2 \cdot v > 0$  then
14:      return  $\ell = 4$  (decel)
15:    end if
16:  end if
17:  if  $R_{\text{lin}}^2 \geq 0.65$  then
18:    return  $\ell = 2$  (linear)
19:  end if
20:  return  $\ell = 6$  (other — deferred to GMM)
21: end if

```

260 **3.5.5 GMM secondary classification**

261 Points unresolved by rules (label = -1) are passed to a Gaussian Mixture Model fitted on
262 the standardised 18-feature space. GMM component means are seeded from the centroids
263 of rule-labelled points:

$$\mu_k^{(0)} = \frac{1}{|C_k|} \sum_{i \in C_k} \mathbf{x}_i \quad (7)$$

264 where C_k denotes the set of rule-classified points for class k . The number of components is
265 $K = 5$. Rule-assigned labels are never replaced; the GMM resolves only the other residual
266 class. Classification outputs written back to `_meta.parquet` are: `class_1`, `class_2`,
267 `class_prob_1` (1.0 for rule-assigned; GMM posterior probability for other), and the four
268 boolean descriptor flags.

269 **3.6 Velocity-weighted 3D DBSCAN clustering**270 **3.6.1 Motivation**

271 Standard 2D spatial clustering (including Euclidean DBSCAN) groups spatially proximate
272 points regardless of their deformation rate. As an example, a cluster spanning both
273 -15 mm yr^{-1} subsiding points and $+2 \text{ mm yr}^{-1}$ stable points has no geophysical meaning.

274 The 3D approach described here ensures that two points are density-connected only when
 275 they are simultaneously spatially proximate and dynamically similar.

276 3.6.2 3D feature space and velocity rescaling

277 The velocity axis is rescaled so that a velocity difference of ε_v mm yr⁻¹ is geometrically
 278 equivalent to ε_m m of spatial separation:

$$w_v = \frac{\varepsilon_m}{\varepsilon_v} \quad (8)$$

279 The 3D input to DBSCAN becomes, therefore:

$$\mathbf{x}_i = \begin{pmatrix} E_i \\ N_i \\ v_i \cdot w_v \end{pmatrix} \in \mathbb{R}^3 \quad (9)$$

280 where E_i, N_i are LAEA easting/northing (m) and v_i is mean LOS velocity (mm yr⁻¹).
 281 The single DBSCAN radius $\varepsilon = \varepsilon_m$ then simultaneously enforces:

$$\sqrt{(E_i - E_j)^2 + (N_i - N_j)^2 + (v_i - v_j)^2 w_v^2} \leq \varepsilon_m \quad (10)$$

282 which is approximately equivalent to requiring both $\sqrt{(E_i - E_j)^2 + (N_i - N_j)^2} \leq \varepsilon_m$ and
 283 $|v_i - v_j| \leq \varepsilon_v$.

284 3.6.3 Algorithm and cluster characterisation

285 Only eligible points are passed to DBSCAN, which satisfy the condition: $|v| \geq v_{\min}$
 286 and $\gamma \geq \gamma_{\min}$ ($v_{\min} = 2.5$ mm yr⁻¹, $\gamma_{\min} = 0.5$ for the demonstrator case). DBSCAN
 287 (Ester et al., 1996) is run with `eps = ε_m` , `algorithm=ball_tree`, `n_jobs=-1` (all cores).
 288 For each resulting cluster, class purity $\rho = n_{\text{dominant}}/n_{\text{total}}$ is computed; clusters below
 289 $\rho_{\min} = 0.5$ are flagged as mixed. Cluster polygons are computed as convex hulls (via
 290 `scipy.spatial.ConvexHull`) buffered by $b_m = 20$ m with rounded cap and join styles
 291 (`resolution=32`), reprojected to EPSG:4326 for output. Cluster IDs follow the format
 292 `CL_nnnn`. Buffering with rounded caps is used to preserve geomorphological consistency
 293 and is based on the local approximate Sentinel-1 pixel resolution.

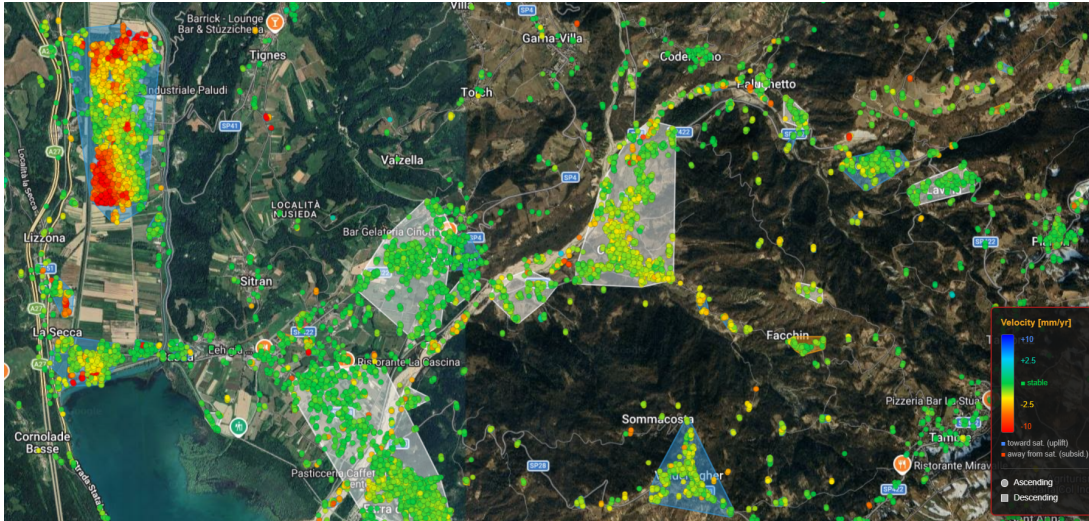


Figure 3: Example output of the velocity-weighted 3D DBSCAN clustering step for a peri-Alpine area in the Belluno province (Veneto, NE Italy). Coloured circles and squares represent InSAR measurement points coloured by mean LOS velocity (red = away from satellite, blue = towards satellite, green = stable) using the official EGMS colour scale. Ascending-orbit points are shown as circles and descending-orbit points as squares. Semi-transparent grey polygons are cluster convex hulls buffered by 20 m, each grouping spatially proximate points within $\varepsilon_m = 100$ m and $\varepsilon_v = 3$ mm yr⁻¹. The red/orange cluster (upper left) corresponds to an industrial area undergoing active subsidence; the smaller clusters across the scene highlight individual buildings, road embankments and hillslope sectors with coherent deformation signals.

294 3.7 Per-class sub-clustering

295 3.7.1 Motivation

296 First-order (or parent) clusters may span large areas and contain spatially distinct deformation
 297 sub-patterns that share similar average velocities but differ in temporal behaviour
 298 or in the kinematics. Sub-clustering stratifies each parent cluster by TS class and runs
 299 a secondary DBSCAN within each stratum (Fig. 4), producing group IDs of the form
 300 CL_nnnn_SUB_mmm. Embedding the parent cluster ID in the sub-cluster ID enables efficient
 301 DuckDB lookups without a join (`WHERE subcluster_id LIKE 'CL_0042%'`). Sub-
 302 clustering may support expert interpretation of deformations measured by InSAR and
 303 help in the correct identification of impending hazards. In case of large slope instabil-
 304 ities, such as deep-seated gravitational slope deformations, sub-clustering may also be
 305 fundamental for landslide parameter estimation, numerical model design, and calibration
 306 (Catani et al., 2016; Bhuyan et al., 2024, 2025).

307 3.7.2 Implementation

308 Eligible points are grouped on the compound key `cluster_id + class_1` using `pandas.groupby`;
 309 per-group DBSCAN tasks are dispatched sequentially, with sub-cluster IDs and convex-
 310 hull polygons accumulated and written back to the `_meta.parquet` files on completion.
 311 Per-group DBSCAN tasks are dispatched as a `joblib` generator with `return_as="generator"`,

312 allowing write-back to begin while remaining groups are still computing. Sub-cluster IDs
 313 and polygon GeoPackage (`subclusters_polygons.gpkg`, EPSG:3035) are produced as
 314 outputs.

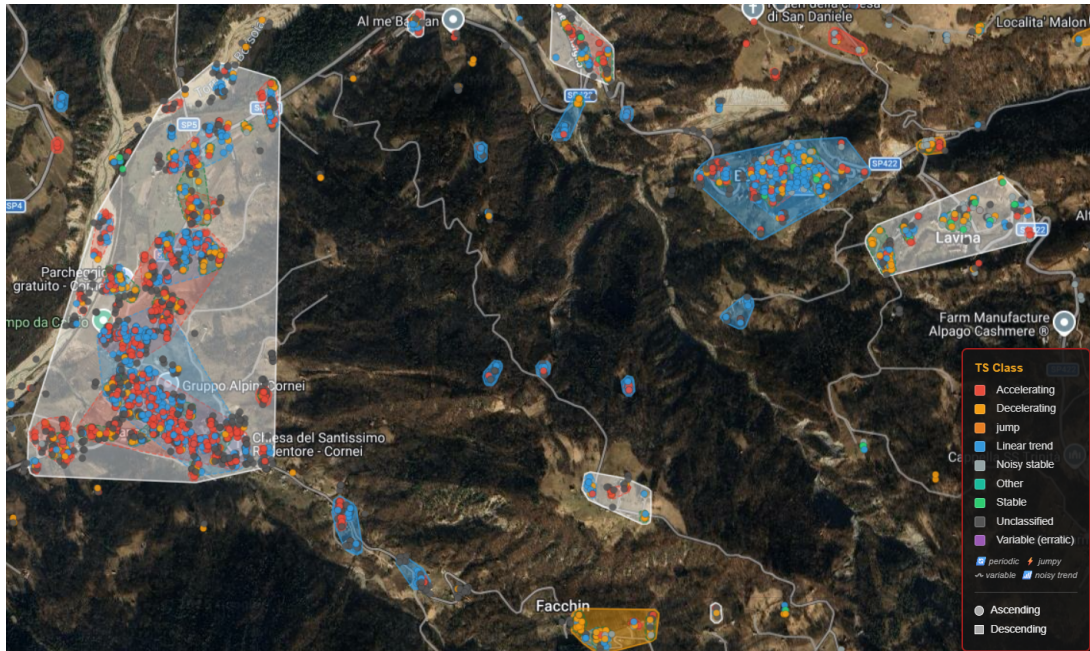


Figure 4: Sub-clustering output for the same peri-Alpine area shown in Fig. 3, with points coloured by time series classification class (red = accelerating, orange = decelerating, blue = linear trend, grey = noisy-stable, green = stable, purple = variable, olive = other). Sub-cluster polygons (semi-transparent fills in matching colours) delineate spatially and behaviourally coherent groups within each parent cluster. The mixture of accelerating (red) and linear (blue) points visible within the large left-hand cluster indicates spatially co-located areas with distinct deformation dynamics, separable only after TS classification. The legend (lower right) also shows the four descriptor flags (*periodic*, *jumpy*, *variable*, *noisy trend*) which are rendered as small icon overlays in the viewer.

315 3.8 DuckDB query layer and web visualisation

316 3.8.1 Flask/DuckDB bridge

317 The visualisation of data, classifications, and clusters is implemented with the combi-
 318 nation of a query system fed by an interactive HTML viewer and a DuckDB database.
 319 The module `bridge.py` is a lightweight Flask server that exposes the DuckDB federated
 320 database to the browser via a REST API (Table 4). All queries run in-memory on a
 321 single persistent `duckdb.connect(":memory:")` instance. The viewport query uses a single
 322 Common Table Expression that computes both the spatially-thinned point set and
 323 the raw count in one execution plan, eliminating the concurrent-connection conflicts that
 324 arise from sequential queries when browser requests are aborted mid-flight:

```
325 WITH filtered AS (  

  326   SELECT * FROM all_metadata  

  327   WHERE latitude BETWEEN :min_lat AND :max_lat
```

```

329     AND longitude BETWEEN :min_lon AND :max_lon
330     AND ABS(mean_velocity) >= :thresh
331     AND temporal_coherence >= :min_coh ),
332 total_cte AS ( SELECT COUNT(*) AS n FROM filtered ),
333 ranked   AS ( SELECT *,
334     ROW_NUMBER() OVER (
335     PARTITION BY FLOOR(latitude/:cell), FLOOR(longitude/:cell)
336     ORDER BY temporal_coherence DESC ) AS _rn
337 FROM filtered ),
338 thinned   AS ( SELECT * FROM ranked WHERE _rn=1 LIMIT :max_pts )
339 SELECT t.*, tc.n FROM thinned t CROSS JOIN total_cte tc
340

```

Table 4: REST API endpoints exposed by `bridge.py`.

Endpoint	Description
GET /get_points	Viewport + filter query with adaptive spatial thinning. Returns JSON array; headers X-Total-Count, X-Rendered-Count.
GET /get_timeseries	Full TS for one pid. Returns dates, values, gap annotations.
GET /get_info	DB statistics and feature flags (<code>has_classes</code> , <code>has_clusters</code> , etc.).
GET /get_clusters	Parent cluster polygons as GeoJSON.
GET /get_subclusters	Sub-cluster polygons as GeoJSON.
GET /health	Liveness check; used by GUI bridge monitor.

341 The spatial thinning grid cell size is zoom-adaptive (Table 5), ensuring that at low zoom
342 levels only the highest-coherence representative per ≈ 13 km cell is returned, while at zoom
343 ≥ 12 the cell size is smaller than the typical PS spacing and all points are returned.

Table 5: Adaptive spatial grid thinning parameters by Leaflet zoom level. At each cell, the point with highest temporal coherence is selected.

Zoom	Cell size (°)	Approximate ground size
5	0.120	≈ 13 km
8	0.015	≈ 1.7 km
10	0.004	≈ 400 m
12	0.001	≈ 100 m
≥ 12	0.001	All points (cell < PS spacing)

344 3.8.2 Canvas-based web viewer

345 `viewer.html` is a single self-contained file embedding Leaflet.js and a custom `EgmsCanvasLayer`
346 renderer (Fig. 5). All points are drawn in a single `requestAnimationFrame` Canvas 2D
347 pass with zero per-point DOM objects or event listeners. During pan, the canvas is shifted
348 via CSS transform with no redraw; full redraw occurs only on `moveend` and `zoomend`.
349 Hit testing uses a 32-pixel spatial grid index ($O(1)$ per click). The hard cap of 200,000
350 rendered points is handled smoothly by the canvas renderer, compared to $\approx 10,000$ for
351 individual Leaflet markers.

352 Ascending-orbit points are rendered as circles and descending-orbit points as squares.
 353 Points are coloured by the official EGMS velocity scale (blue = uplift, green = stable,
 354 yellow/red = subsidence) or, optionally, by time series class. Ctrl+clicking multiple points
 355 opens overlapping time series in a floating panel with up to ten distinguishable colours.



Figure 5: The MISSlab EGMS web viewer showing a portion of the Belluno–Alpago area (NE Italy, Veneto/Friuli-Venezia Giulia border). Points are coloured by time series class (legend, lower right); ascending-orbit points (Sentinel-1 tracks 015–139) are shown as circles and descending-orbit points (tracks 146–168) as squares. The viewer is displaying 23,641 points at zoom level 12 with $|v| \geq 3 \text{ mm yr}^{-1}$ and coherence ≥ 0.5 filters applied; the status bar (top left) shows the current filter state. The toolbar provides controls for velocity/class colour mode, coherence threshold, velocity scale, orbit selection, and cluster/sub-cluster polygon overlay. The viewer supports sub-100 ms viewport queries over the full ≈ 300 M-point northern Italy database via the DuckDB/Flask bridge, enabling real-time interactive exploration comparable to a desktop GIS but without data subsampling.

356 4 Results

357 4.1 Pipeline quality control: velocity consistency

358 As an internal consistency check, we compared the EGMS pre-computed mean LOS ve-
 359 locity (`mean_velocity`, derived from the official EGMS weighted least-squares processing
 360 chain) against the OLS velocity independently recomputed by EGMSpy from the stored
 361 float32 time series. A random sample of 99,751 points was drawn from all 433 tile pairs
 362 and the two estimates compared (Fig. 6).

363 The two velocity estimates agree to within $\text{RMSE} = 0.096 \text{ mm yr}^{-1}$, $\text{bias} = -0.001 \text{ mm yr}^{-1}$,
 364 Pearson $r = 0.9993$. Zero points in the sample deviated by more than 1 mm yr^{-1} . The

365 residual distribution is symmetric, centred at zero, and narrow — consistent with float32
 366 quantisation noise (± 0.06 mm per value, propagating to ≈ 0.1 mm yr $^{-1}$ in the OLS slope
 367 depending on time span). Panel (c) of Fig. 6 shows a horizontal residual band across
 368 the full velocity range $[-10, +10]$ mm yr $^{-1}$, confirming the absence of velocity-dependent
 369 systematic bias that would indicate errors in the winter-gap interpolation or the float32
 370 conversion. The RMSE of 0.096 mm yr $^{-1}$ is one order of magnitude below the EGMS L2b
 371 measurement precision (≈ 0.5 – 1.0 mm yr $^{-1}$; Crosetto et al. 2020).

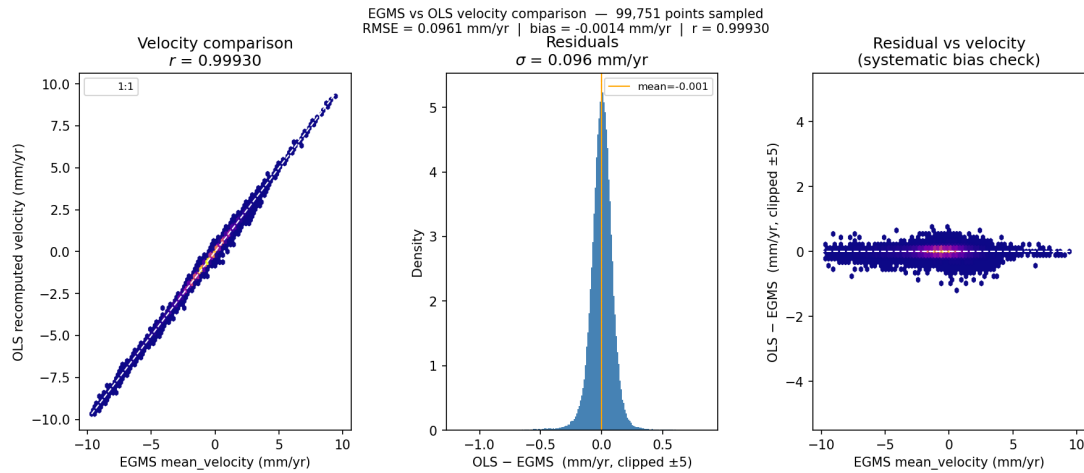


Figure 6: Internal quality check: comparison between the EGMS pre-computed mean LOS velocity and the OLS velocity recomputed by EGMSpy from the stored float32 time series, for a random sample of 99,751 points across all 433 northern Italy tiles (Copernicus EGMS L2b, 2019–2023). (a) Hexbin scatter (yellow = maximum density) showing near-perfect 1:1 agreement ($r = 0.9993$). (b) Residual distribution $\Delta v = v_{\text{OLS}} - v_{\text{EGMS}}$ ($\sigma = 0.096$ mm yr $^{-1}$, bias = -0.001 mm yr $^{-1}$); the sharp symmetric peak is characteristic of float32 quantisation noise. (c) Residuals vs. EGMS velocity, confirming no velocity-dependent bias across the full range. The RMSE is an order of magnitude below EGMS measurement precision (≈ 0.5 – 1.0 mm yr $^{-1}$; Crosetto et al. 2020), validating the toolkit’s internal feature extraction and confirming that the winter-gap correction introduces no detectable velocity artefact.

372 4.2 Classification and clustering results

373 4.2.1 Demonstrator dataset overview

374 The northern Italy EGMS L2b database (2019–2023) processed with EGMSpy com-
 375 prises **282,606,853 coherent scatterers** across 433 tile pairs, distributed nearly equally
 376 between ascending (137,713,488 points; 48.7%) and descending (144,893,365; 51.3%)
 377 Sentinel-1 geometries. The mean temporal coherence is $\bar{\gamma} = 0.756$ (median = 0.77), re-
 378 flecting the predominantly urban and agricultural character of the Po Plain and pre-Alpine
 379 foothills where coherence is maintained across the full 2019–2023 observation period.

380 The overall velocity distribution is negatively skewed (mean = -0.93 mm yr $^{-1}$, median
 381 = -0.8 mm yr $^{-1}$, $\sigma = 1.98$ mm yr $^{-1}$), with a markedly asymmetric tail: the 5th percentile
 382 (-3.5 mm yr $^{-1}$) lies $3.2\times$ further from zero than the 95th percentile ($+1.1$ mm yr $^{-1}$). This

negative bias is a robust signal of widespread, low-rate subsidence across the study area, consistent with the well-documented Po Plain groundwater-driven consolidation (Colesanti et al., 2003; Raspini et al., 2019; Chen et al., 2026) and with the general tendency for InSAR LOS velocities in this region. Extreme velocities reach -101.5 and $+98.4$ mm yr^{-1} , with 1,588,542 points (0.56%) exceeding $|v| \geq 10$ mm yr^{-1} , indicative of localised rapid deformation such as active landslides, mining subsidence, and infrastructure settlement.

4.2.2 Time series classification

Of the 282,606,853 processed points, 276,281,109 (97.8%) were assigned a primary class label by the EGMSpy classifier; the remaining 2.2% remain unclassified, predominantly in Alpine areas with short valid time series ($n_{\text{valid}} < 10$ acquisitions) or extreme velocity outliers that fell outside all rule boundaries. Table 6 summarises the full class distribution.

Table 6: Time series classification results for the northern Italy EGMS L2b dataset (282,606,853 points, 433 tiles). Percentages refer to the total point count. Velocity statistics are given for each class.

Class	N	%	\bar{v}	σ_v	v_{P05}	v_{P95}
				(mm yr^{-1})		
noisy-stable	148,002,066	52.4	-0.53	1.07	-2.2	+1.3
stable	103,877,470	36.8	-0.77	0.90	-2.2	+0.7
linear	16,293,143	5.8	-4.80	3.53	-10.9	-2.5
accel	4,473,766	1.6	-2.75	1.92	-4.7	+2.8
decel	3,634,636	1.3	-2.67	2.00	-4.7	+2.9
unclassified	6,325,744	2.2	-0.60	7.14	-7.5	+2.9
Total	282,606,853	100				

Stable and noisy-stable classes. The dominant classes are *noisy-stable* (52.4%) and *stable* (36.8%), together accounting for 89.1% of all points. Both classes are confined by definition to $|v| < v_s = 2.5$ mm yr^{-1} , and their velocity distributions are broadly similar (mean -0.53 and -0.77 mm yr^{-1} respectively). The distinction between them is the residual scatter after linear detrending: *stable* points have low scatter ($\text{rmse_dt} \leq 3.0$ mm), while *noisy-stable* points exceed this threshold. The high proportion of *noisy-stable* points reflects the abundance of partly-coherent scatterers in agricultural and vegetated areas at the margins of the stable PS network, where temporal decorrelation introduces scatter without a systematic trend.

Unstable classes. Points classified as *linear*, *accel*, or *decel* together comprise 24,401,545 points (8.8% of classified points; Table 6). The *linear* class ($n = 16,293,143$; 5.8%) has a strongly negative mean velocity (-4.80 mm yr^{-1} , $P50 = -4.1$ mm yr^{-1}) with a negative-only 95th-percentile range ($v_{P95} = -2.5$ mm yr^{-1}), confirming that the vast majority of linearly-trending points represent steady subsidence. The *accel* class ($n = 4,473,766$; 1.6%) and *decel* class ($n = 3,634,636$; 1.3%) show similar velocity distributions (mean ≈ -2.7 mm yr^{-1}), with the slight excess of accelerating over decelerating points (ratio 1.23:1) consistent with an ongoing consolidation trend that began before the observation

411 window and has not yet reached equilibrium in many locations. Both classes exhibit wide
 412 95th-percentile ranges that span into positive velocities, indicating that non-subsidence
 413 phenomena (slope failures, localised uplift, frost heave, permafrost degradation, infras-
 414 tructure rebound) also contribute to these classes.

415 **Descriptor flags.** Table 7 summarises the four boolean descriptor flags, which are
 416 independent of and combinable with the primary class.

Table 7: Descriptor flag statistics. Flags are assigned independently of primary class and may co-occur with each other and with any primary class. Percentages refer to the total 282,606,853 classified points and sum to more than 100% because multiple flags may be set simultaneously on a single point.

Flag	N	%	Interpretation
jumpy	178,877,339	63.3	≥ 1 abrupt step ≥ 5 mm
variable_flag	86,707,933	30.7	High CUSUM changepoint score
periodic	66,842,068	23.7	Significant annual/semi-annual harmonic
noisy_trend	9,983,537	3.5	Moving point with high residual scatter

417 The **jumpy** flag (63.3%) deserves careful interpretation: given that the *noisy-stable* class
 418 constitutes 52.4% of all points, and noisy time series intrinsically contain large first differ-
 419 ences that may exceed the fixed 5 mm jump threshold, a substantial fraction of the **jumpy**
 420 flags in the noisy class represent measurement scatter rather than true geophysical step
 421 events. True geophysical jumps are more reliably identified when the **jumpy** flag co-occurs
 422 with *linear*, *accel*, or *decel* classes. The **periodic** flag (23.7%) indicates that nearly one in
 423 four coherent scatterers in northern Italy show a statistically significant annual or semi-
 424 annual harmonic component in its displacement time series, reflecting the region’s strong
 425 seasonal groundwater fluctuations, agricultural irrigation cycles, and frost-heave signals
 426 in the peri-Alpine zone. The **variable_flag** (30.7%) captures points with erratic rate
 427 changes — a population that includes both geophysically meaningful episodic deformation
 428 (e.g. triggered landslide acceleration) and measurement artefacts from atmospheric phase
 429 screen residuals (Zebker et al., 1997), i.e. spatially-correlated tropospheric delay errors
 430 not fully removed during InSAR processing.

431 4.2.3 Spatial patterns of deformation across geomorphological zones

432 The dataset is partitioned into three elevation-based physiographic zones following the
 433 standard Italian geomorphological classification (Fredi and Lupia Palmieri, 2004): the
 434 plain and low-hill zone (point elevation < 600 m a.s.l., comprising the Po Plain, the Vene-
 435 tian lowland, and the Ligurian and Apennine foothills), the mid-mountain zone (600–
 436 1500 m), and the high-mountain zone (> 1500 m, corresponding to the Alpine chain proper
 437 and high Apennine crests). Table 8 reports the class distribution and velocity statistics
 438 per zone; the three zones reveal markedly different deformation regimes consistent with
 439 the known geomorphology of northern Italy.

Table 8: Class distribution and velocity statistics by physiographic zone. Zone boundaries follow the standard Italian geomorphological classification (Fredri and Lupia Palmieri, 2004): plain and low hill (< 600 m a.s.l.), mid-mountain (600–1500 m), high mountain (> 1500 m). Only classes with >0.1% zonal frequency are listed. \bar{v} and σ_v in mm yr^{-1} .

Zone	Class	N	% _{zone}	\bar{v}	σ_v	v_{P05}	v_{P95}
Plain / low hill	noisy-stable	107,145,817	46.6	-0.75	1.01	-2.3	+1.0
	stable	97,846,072	42.6	-0.80	0.88	-2.2	+0.7
	linear	14,976,656	6.5	-4.81	2.92	-10.6	-2.6
	accel	4,034,150	1.8	-2.90	1.69	-4.7	+2.6
	decel	3,199,778	1.4	-2.84	1.72	-4.6	+2.6
Mid-mountain	noisy-stable	16,386,357	68.9	-0.23	1.06	-2.0	+1.5
	stable	4,881,279	20.5	-0.35	1.05	-2.0	+1.3
	linear	782,216	3.3	-4.12	5.55	-12.3	+5.4
	accel	265,163	1.1	-1.79	2.77	-4.5	+3.5
	decel	275,040	1.2	-1.75	3.05	-5.0	+3.8
High mountain	noisy-stable	24,469,892	83.9	+0.24	0.94	-1.3	+1.7
	stable	1,150,119	3.9	+0.12	1.48	-3.2	+2.5
	linear	534,271	1.8	-5.45	9.66	-21.3	+6.2
	accel	174,453	0.6	-0.58	3.23	-4.6	+3.4
	decel	159,818	0.5	-0.91	3.20	-4.7	+3.4

440 **Plain and low-hill zone (< 600 m a.s.l.; 229,682,099 points, 81.3% of total).**
441 This zone dominates the dataset by point count, reflecting the high PS density in urban
442 and agricultural areas of the Po Plain and Po delta lowland where temporal coherence
443 is well maintained over the full 2019–2023 observation window. The *linear* class reaches
444 its highest zonal proportion here (6.5%), with a strongly negative velocity distribution
445 ($\bar{v} = -4.81 \text{ mm yr}^{-1}$; $P95 = -2.6 \text{ mm yr}^{-1}$) — the entire upper 5th percentile of the distri-
446 bution remains in land affected by subsidence. This pattern reflects the well-documented
447 ongoing consolidation of Holocene alluvial deposits throughout the Po Plain (Colesanti
448 et al., 2003; Teatini et al., 2005; Raspini et al., 2019), amplified by groundwater over-
449 exploitation in agricultural and urban areas. The *accel* class (1.8%) has a mean velocity
450 of -2.90 mm yr^{-1} , indicating that accelerating deformation in this zone is predominantly
451 confined to the subsidence domain, consistent with progressive alluvial deposits consoli-
452 dation rather than gravity-driven kinematics. The overall velocity bias in this zone is the
453 strongest of the three ($\bar{v}_{\text{noisy}} = -0.75 \text{ mm yr}^{-1}$, $\bar{v}_{\text{stable}} = -0.80 \text{ mm yr}^{-1}$), confirming that
454 even nominally stable scatterers show a measurable systematic downward motion relative
455 to the GNSS reference frame.

456 **Mid-mountain zone (600–1500 m a.s.l.; 23,770,476 points, 8.4% of total).** The
457 mid-mountain zone is characterised by a strong shift toward noise-dominated signals: the
458 *noisy-stable* class reaches 68.9%, substantially higher than in the plain but lower than
459 in the high-mountain zone, reflecting the intermediate InSAR conditions of peri-Alpine
460 valleys, Apennine ridges, and lower Alpine slopes where partial vegetation cover and
461 seasonal snow reduce but do not eliminate coherence. The *linear* proportion (3.3%) is

462 lower than in the plain, and its velocity distribution is markedly wider ($\sigma_v = 5.55 \text{ mm yr}^{-1}$,
 463 $P05 = -12.3 \text{ mm yr}^{-1}$, $P95 = +5.4 \text{ mm yr}^{-1}$), spanning both subsiding and uplifting
 464 signals. This reflects the geomorphological diversity of the zone, which encompasses slow
 465 valley-floor subsidence, active slope deformation on Apennine and peri-Alpine hillsides,
 466 and localised deep-seated deformation signals, partly linked to debuttressing. The *accel*
 467 and *decel* classes are roughly balanced (1.1% vs. 1.2%), suggesting a population of slopes in
 468 different phases of kinematic activity, from reactivating landslides to seasonally modulated
 469 creep. Notably, the *jumpy* flag rate in this zone (71.8%) is the highest of the three,
 470 reflecting both phase unwrapping difficulties over high-relief terrain and genuine abrupt
 471 displacement events on steep slopes.

472 **High-mountain zone (> 1500 m a.s.l.; 29,154,278 points, 10.3% of total).** The
 473 high-mountain zone shows the most extreme classification pattern, with 83.9% of points
 474 assigned to the *noisy-stable* class — the highest fraction of any zone — and only 3.9%
 475 *stable*. This reflects the severe InSAR conditions above the snow line: rocky terrain with
 476 few artificial reflectors, persistent winter snow cover causing temporal decorrelation, and
 477 strong atmospheric phase screen residuals from orographic precipitation and vertical tro-
 478 pospheric gradients (Zebker et al., 1997). Critically, the *noisy* class in this zone has a near-
 479 zero mean velocity ($\bar{v} = +0.24 \text{ mm yr}^{-1}$) with a symmetric, narrow range ($P05 = -1.3$,
 480 $P95 = +1.7 \text{ mm yr}^{-1}$), in marked contrast to the systematic negative bias observed in both
 481 lower zones. This confirms that the high-mountain *noisy-stable* points are dominated by
 482 measurement noise rather than real deformation signals. The *linear* class (1.8%) shows the
 483 widest velocity spread of any class-zone combination ($\sigma_v = 9.66 \text{ mm yr}^{-1}$; $P05 = -21.3$,
 484 $P95 = +6.2 \text{ mm yr}^{-1}$), reflecting a heterogeneous population that includes fast-moving
 485 rockslide and DSGSD complexes, glacially influenced subsidence, periglacial frost-heave
 486 signals, and debuttressing. The *periodic* flag drops sharply from 25.5% in the plain zone
 487 to 10.9% in the high-mountain zone, consistent with the reduced contribution of infras-
 488 tructure thermal deformation and groundwater-driven seasonal signals at high elevation.

489 5 Discussion

490 5.1 Geoscientific interpretation of deformation patterns

491 The classification of 282 M EGMS L2b coherent scatterers across northern Italy reveals
 492 a spatially organised pattern of ground deformation styles that is consistent with the
 493 regional geology and known geohazard inventory, providing a first-order validation of the
 494 EGMSpy classification scheme.

495 **Systematic negative velocity bias and Po Plain consolidation.** The most perva-
 496 sive result is the negative velocity bias of the entire dataset ($\bar{v} = -0.93 \text{ mm yr}^{-1}$) and the
 497 $3.2\times$ longer negative tail of the velocity distribution ($P05 = -3.5$ vs $P95 = +1.1 \text{ mm yr}^{-1}$).
 498 This asymmetry is a well-established physical signal of widespread, low-rate subsidence
 499 across the study area, driven by the compaction of Quaternary alluvial sediments under
 500 the combined influence of natural consolidation, groundwater extraction, and hydrocar-
 501 bon production (Colesanti et al., 2003; Teatini et al., 2005; Cenni et al., 2021). The
 502 spatial gradient — from near-zero mean velocity in the high-mountain zone through the

503 mid-mountain transition to the plain and low-hill zone (systematic $\approx -0.8 \text{ mm yr}^{-1}$ even
504 in nominally stable scatterers) — is captured by the elevation-zone analysis without any
505 a priori spatial constraint.

506 The dominance of the *linear* class in the plain and low-hill zone (6.5% of zone points,
507 vs. 3.3% mid-mountain and 1.8% high-mountain) and its strongly negative velocity dis-
508 tribution ($\bar{v} = -4.81 \text{ mm yr}^{-1}$, with the entire 90th-percentile range remaining negative)
509 are in close agreement with dedicated InSAR time series analyses of the same area. **Chen**
510 **et al. (2026)** analysed EGMS Sentinel-1 data over the Po River Delta (a sub-region of
511 our Po Plain zone) using a regression-based decomposition approach and found that the
512 temporal behaviour of most PS points is *trend-dominated* — the equivalent of our *linear*
513 class — with subsidence rates consistent with ongoing Holocene sediment compaction.
514 Their spatial modelling of subsidence as a function of Holocene deposit age fitted a log-
515 arithmic relationship ($R^2 = 0.72$), confirming that natural consolidation is the dominant
516 first-order control on Po Plain subsidence rates, with deviations from the modelled curve
517 attributable to localised anthropogenic drivers such as groundwater extraction and infras-
518 tructure loading. Our median velocity for plain-zone *linear*-class points (-4.1 mm yr^{-1})
519 falls within the range predicted by **Chen et al. (2026)** logarithmic model for sediments
520 of intermediate Holocene age ($\approx 1,000\text{--}3,000 \text{ yr BP}$), and our P05 (-10.6 mm yr^{-1}) cor-
521 responds to rates expected from the most recent deltaic deposits ($< 500 \text{ yr BP}$), where
522 compressibility and consolidation rates are highest.

523 **Accelerating and decelerating deformation.** The slight excess of *accel* over *de-*
524 *cel* points across the dataset (1.6% vs. 1.3%; ratio 1.23:1) is consistent with an ongoing
525 but non-equilibrium consolidation process: subsidence is still predominantly accelerating
526 rather than decelerating throughout most of the Po Plain, suggesting that the pertur-
527 bations driving enhanced consolidation (groundwater abstractions, land reclamation, in-
528 frastructure loading) continue to outpace natural relaxation. In the plain and low-hill
529 zone specifically, the mean velocity of the *accel* class (-2.90 mm yr^{-1}) confirms that ac-
530 celerating deformation is predominantly confined to the subsidence domain. **Chen et al.**
531 **(2026)** similarly found that abrupt changes detected by the BEAST algorithm along Po
532 Delta levees are most often consistent with accelerated consolidation under structural
533 loading, particularly where new road surfaces and built infrastructure have been added
534 to unconsolidated deltaic deposits.

535 **Seasonal signals: infrastructure vs. natural terrain.** The periodic flag assigned
536 to 23.7% of all points documents the pervasiveness of annual and semi-annual harmonic
537 components in the displacement time series across the study area. However, the physical
538 origin of this signal varies substantially by scatterer type. **Chen et al. (2026)** provide a key
539 disambiguation: in the Po Delta, seasonal displacement signals are strongly concentrated
540 on metal infrastructure — bridges and transmission towers — whose apparent deformation
541 reflects thermal expansion and contraction of structural elements rather than true ground
542 motion. Their analysis shows that bridge end-points can exhibit opposing correlations
543 with land surface temperature (one end positive, the other negative), attributed to the
544 differential thermal response along the bridge span. In natural terrain, the seasonal signal
545 is primarily driven by pore pressure fluctuations associated with groundwater recharge

546 cycles and, in peri-Alpine and Alpine areas, by local hydrological oscillations, freeze-
547 thaw cycles, and snow loading effects. This distinction implies that a fraction of the
548 23.7% **periodic** points in our dataset are infrastructure scatterers responding to thermal
549 forcing rather than recording hydrogeological or geotechnical ground motion. Separating
550 these two populations — for example, by cross-referencing the **periodic** flag with land-
551 use or infrastructure datasets — could be an useful future development to improve the
552 geomorphological interpretability of the seasonal signal.

553 **High-mountain zone: noise dominance and high-velocity outliers.** The high-
554 mountain zone’s 83.9% *noisy-stable* fraction, near-zero mean velocity ($+0.24 \text{ mm yr}^{-1}$),
555 and symmetric velocity distribution confirm that this zone is dominated by measure-
556 ment noise rather than geophysical signal, consistent with the severe InSAR conditions
557 above the permanent snow line (Zebker et al., 1997). However, the *linear* class in the
558 high-mountain zone shows the highest velocity standard deviation of any class-zone com-
559 bination ($\sigma_v = 9.66 \text{ mm yr}^{-1}$) and the widest P05–P95 range (-21.3 to $+6.2 \text{ mm yr}^{-1}$),
560 indicating a heterogeneous population of scattered, low-autocorrelation clusters that in-
561 clude both slow-moving landslides and deep-seated gravitational slope deformation (DS-
562 GSD) complexes alongside glacially-influenced motion. This heterogeneity in the *linear*
563 class is consistent with the findings of Dong et al. (2025), who used a multimodal deep
564 learning approach to classify EGMS-derived active deformation areas (ADAs) across Italy
565 into four geophysical process types (landslide, subsidence, DSGSD, mining). Their classi-
566 fication of 99,402 Italian ADAs — identifying 71,101 landslides, 18,853 subsidence areas,
567 5,191 mining sites, and 4,257 DSGSDs — showed that mountainous regions with steep
568 slopes and high elevations (as in our Alpine zone) are predominantly associated with
569 landslide and DSGSD processes. Their explainable AI analysis further revealed that the
570 two processes are the most commonly confused pair, with 84 misclassification cases on
571 the ascending dataset, consistent with the inherent geomorphological similarity between
572 deep-seated and shallow slope deformation at the millimetre-per-year displacement rates
573 captured by EGMS.

574 5.2 Complementarity with existing classification frameworks

575 **Time series pattern classification vs. process classification.** EGMSpy’s classi-
576 fication scheme assigns *time series behaviour labels* (stable, noisy-stable, linear, accel,
577 decel, variable) to individual PS points. This is distinct from, and complementary to,
578 the *geophysical process classification* approach of Dong et al. (2025), who assign process
579 labels (landslide, subsidence, DSGSD, mining) to spatially coherent deformation clusters
580 (ADAs) with supervised classification. The two approaches operate at different scales
581 and use different information: EGMSpy uses per-point kinematic features extracted from
582 the displacement time series alone, while the approach of Dong et al. (2025) additionally
583 leverages DEM, slope, aspect, and optical imagery to capture the morphological context
584 of each deforming area. Their ablation study demonstrates that TS information alone
585 achieves only $\approx 61\%$ mean F1 on the ascending dataset, while spatial and morphological
586 features alone reach $\approx 81\%$, with the multimodal fusion achieving $>91\%$ overall accuracy.
587 This result motivates a natural extension of EGMSpy: the cluster polygons produced by
588 the velocity-weighted 3D DBSCAN step are direct analogues of ADAs, and could serve

589 as the spatial units for a subsequent process-level classification step that incorporates
590 DEM and land-cover variables. Such an integration would enable a seamless two-stage
591 pipeline from raw EGMS data to geophysical process labels: EGMSpy handles the data
592 management, time series characterisation, and clustering stages, while a process classifier
593 such as that of [Dong et al. \(2025\)](#) would operate on the resulting cluster geometries.

594 **Anomaly detection and critical infrastructure monitoring.** The jumpy descrip-
595 tor flag identifies points with abrupt displacement steps in their time series, a population
596 that includes both genuine geophysical change points (e.g. triggered accelerations, levee
597 deformation events) and measurement artefacts (phase unwrapping errors, processing dis-
598 continuities). [Chen et al. \(2026\)](#) demonstrate that the BEAST Bayesian change-point al-
599 gorithm can reliably separate real from artefactual breaks in Po Delta PS time series, with
600 posterior probabilities > 0.9 providing a conservative criterion for true structural change.
601 In their study, BEAST-detected change points cluster spatially along levees, embank-
602 ments, and urbanised areas, while geologically quiet zones show few significant breaks.
603 This spatial pattern is directly consistent with the expected distribution of the jumpy flag
604 in our dataset: if the flag were re-examined at a spatial scale (i.e., what fraction of flagged
605 points lie along known infrastructure vs. natural terrain), the infrastructure-associated
606 fraction would likely dominate. The high overall jumpy rate (63.3%) we observe across
607 the full northern Italy dataset warrants careful interpretation, as noted in Section 4.2: a
608 large fraction reflects noise in the *noisy-stable* class rather than true step events. Future
609 work will apply probabilistic change-point detection analogous to [Chen et al. \(2026\)](#) to
610 filter the jumpy population and identify the subset of infrastructure-associated change
611 points with genuine monitoring significance.

612 5.3 Comparison with existing tools

613 It is useful to compare EGMSpy processing algorithms with those of existing available
614 tools of similar scope and range. Table 9 summarises the capabilities of EGMSpy relative
615 to tools commonly used for InSAR time series analysis and EGMS data access. The
616 approaches of [Chen et al. \(2026\)](#) and [Dong et al. \(2025\)](#) are included for context, as they
617 operate on the same EGMS data source.

Table 9: Capability comparison with related tools and approaches operating on Copernicus EGMS data. TS = time series; ADA = active deformation area.

Tool / Study	Scope	$N > 10^7$	Key characteristic
EGMS Explorer portal	Single-tile viewer	No	No classification, no multi-tile query
EGMStoolkit (Hrysiewicz et al., 2024) Chen et al. (2026)	Download utility Regional (Po Delta)	No Partial	Download only; no analysis TS pattern classification + BEAST anomaly detection; spatial subsidence modelling by deposit age
Dong et al. (2025)	National (Italy)	No	Process classification (landslide/subsidence/DSGSD/mining) via multimodal CNN-LSTM fusion on ADAs
MintPy (Yunjun et al., 2019)	Upstream processing	Partial	Raw SLC \rightarrow TS; not applicable to EGMS product
EGMSpy (this work)	Regional to continental	Yes	End-to-end data handling, per-point TS classification, 3D DBSCAN clustering, interactive web viewer; complements Chen et al. 2026 and Dong et al. 2025

618 5.4 Scalability and hardware requirements

619 The current implementation processes the 282 M-point northern Italy dataset on a single workstation (AMD Threadripper 3970X, 274 GB RAM) without distributed computing. The dominant bottleneck is time series classification (≈ 24 – 48 h for 434 tiles at 32 620 joblib workers), which is tile-parallel. DuckDB viewport queries over the full in-memory 621 database complete in 30–80 ms regardless of dataset size, providing a smooth visualisation 622 and management for users. 623 624

625 Scaling to the full EGMS dataset (≈ 5 B points, $\sim 10,000$ tiles) will require migration to GPU-accelerated DBSCAN and GMM (RAPIDS cuML) on a multi-GPU server, with 626 DuckDB Parquet predicate pushdown via a sidecar spatial bounding-box index for tile 627 skipping. The split-GeoParquet tile-per-file architecture is designed to support this transition without any schema changes. However, this kind of application is beyond the scope 628 of the present paper. 629 630

631 A critical performance note: NumPy must be MKL-linked (not OpenBLAS) on AMD 632 platforms. The OpenBLAS default in the conda-forge channel produces a $\approx 40\times$ slow-down in the feature extraction batch OLS on the Threadripper workstation. 633

634 5.5 Limitations and possible developments

635 **Absolute vs. relative jump thresholds.** Jump and noise detection thresholds are
636 currently fixed at 5 mm. Fast-moving points ($|v| > 30 \text{ mm yr}^{-1}$) may have intrinsically
637 larger first differences, causing under-detection of real geophysical jumps. A relative
638 threshold normalised by local velocity magnitude is planned in the next releases. In the
639 meantime, interested users are encouraged to try out different thresholds to experiment
640 model sensitivity.

641 **Winter gap correction.** Acquisition gaps (predominantly November–March in Alpine
642 regions) are filled with linear interpolation. A model-driven approach based on regional
643 groundwater or snow-depth climatology would be more physically consistent and could
644 reduce the *noisy-stable* fraction in Alpine areas. We have also experimented different
645 parameters for gap detection and correction in longer-winter regions, such as Iceland, with
646 notable improvements in the model capability to correctly classify winter gap-affected TS.

647 **Probabilistic change-point detection.** In the next releases of EGMSpy, we plan to
648 supplement the binary *jumpy* flag with probabilistic change-point estimates, following the
649 Bayesian approach demonstrated by [Chen et al. \(2026\)](#) for the Po Delta. This will enable
650 infrastructure monitoring applications analogous to their levee-surveillance framework.

651 **Process-level classification.** The cluster polygons produced by EGMSpy’s 3D DB-
652 SCAN provide a natural input for a subsequent process-level classification stage. In-
653 tegration with the multimodal CNN–LSTM framework of [Dong et al. \(2025\)](#), or similar
654 approaches, which incorporate DEM, slope, and optical imagery, is planned to enable end-
655 to-end labelling from raw EGMS tiles to geophysical process types (landslide, subsidence,
656 DSGSD, mining, or more detailed categories).

657 **Cross-orbit integration.** Ascending and descending LOS velocities are currently pro-
658 cessed independently. Fusion into vertical and east–west displacement components ([Bovenga
659 et al., 2012](#); [Farolfi et al., 2019](#)) is planned for the next release.

660 **Validation.** A rigorous validation of the time series classification against the Italian
661 official landslide inventory and hazard zoning (PAI/IFFI), ground-truth surveys, other
662 available InSAR and GB-InSAR time series, and GNSS time series to quantify spatial
663 information as in [Catani et al. \(2016\)](#) is being done in the framework of a scientific coop-
664 eration between the District Authority of the Po River, the University of Modena-Reggio
665 Emilia, the University of Bologna, the CNR-IRPI Turin, the University of Milan Bicocca,
666 the University of Pavia, and the University of Padova across all the areas encompassing the
667 Po river hydrographic basin. Comparisons are also being prepared with EGMS data from
668 areas outside the river basin boundary (North Tuscany, Belluno province, Dolomites).
669 The results of this independent work will be presented in internal technical reports and,
670 possibly, in a follow-up publication.

AI assistance declaration: AI-assisted writing tools were used for copy editing of this manuscript, comprising improvements to grammar and formatting, in accordance with Springer Nature’s editorial policy. All original text, scientific content, data analysis, results, and interpretations are the sole work and responsibility of the human authors.

6 Conclusions

We have presented MISSlab EGMSpy, an open-source Python pipeline for end-to-end processing, classification, clustering and interactive visualisation of Copernicus EGMS L2b ground motion data at regional scale. The key innovations are: (i) a split-GeoParquet with DuckDB storage architecture that enables sub-100 ms analytical queries over hundreds of millions of points on commodity hardware; (ii) a physics-informed hybrid rule/GMM time series classifier that assigns geophysically interpretable labels to every InSAR point without requiring manual parameter tuning; (iii) a velocity-weighted 3D DBSCAN clustering algorithm that identifies spatially and dynamically coherent deformation areas; and (iv) a canvas-based interactive web viewer capable of rendering 200,000+ classified points in a single draw call.

Internal quality control on a random sample of 99,751 northern Italy measurement points confirms that the toolkit’s OLS feature extraction is consistent with the official EGMS pre-computed velocities to within 0.096 mm yr^{-1} RMSE — one order of magnitude below the EGMS measurement precision — with no systematic bias across the full velocity range.

Full quantitative results for the northern Italy dataset (≈ 300 M points) and geoscientific interpretation will be presented in a companion application paper (in preparation).

6 Availability and Requirements

- **Project name:** EGMSpy
- **Project home page:** <https://github.com/fcatani/EGMSpy> (Beta v.1.0)
- **Operating system(s):** Windows 10/11, Linux (Ubuntu 22.04)
- **Programming language:** Python 3.12
- **Required packages:** pandas, geopandas, pyarrow, duckdb, scikit-learn, scipy, shapely, tqdm, pyqt6, flask, flask-cors, fiona, gdal, joblib (all via conda-forge); plotly, kaleido, concave-hull (via pip)
- **Minimum hardware:** 8 GB RAM, multi-core CPU. For >50 M points: ≥ 64 GB RAM recommended. Production runs (>200 M points): ≥ 128 GB RAM, 32+ cores
- **Licence:** MIT
- **Any restrictions to use by non-academics:** None

6 Data and code availability

EGMS L2b data are freely available from the Copernicus Land Monitoring Service (<https://egms.land.copernicus.eu/>) subject to the Copernicus Data Policy. The MISSlab

704 EGMSpy source code is released under the MIT licence at <https://github.com/fcatani/>
 705 EGMSpy (repository in beta version 1.0).

706 6 Statements and Declarations

707 **Funding and Acknowledgements.** This work was partially supported by the District
 708 Authority of the Po River (AdBPo), through the cooperation grant 2023-2027 (“Appro-
 709 fondimento tecnico-scientifico inerente all’uso operativo di dati EGMS negli strumenti di
 710 pianificazione PAI dell’Autorità di bacino distrettuale del Fiume Po”). We sincerely thank
 711 Tommaso Simonelli from AdBPo for the support, suggestions, and continuous exchanges.
 712 We also thank Matteo Berti from the University of Bologna for the early adoption of the
 713 DBSCAN clustering methodology and for the useful confrontation on operational results
 714 in different areas of the Po river basin.

715 **Competing interests.** The authors declare no competing interests.

716 **Author contributions.** F.C.: conceptualisation, methodology, software development,
 717 data curation, formal analysis, writing, original draft, review and editing; C.P.: data
 718 preparation, review, and editing; R.T.: data preparation, review, and editing; L.N: formal
 719 analysis, review, and editing; M.F.: InSAR methodology and data curation, review, and
 720 editing.

721 A Pipeline performance benchmarks

Table 10: Observed and estimated runtimes for the northern Italy dataset (433 tile pairs, ≈ 300 M points) on the AMD Threadripper 3970X workstation (274 GB RAM, MKL-linked NumPy, Windows High Performance power plan).

Step	Runtime	Notes
Download (517 tiles, ≈ 180 GB)	~ 3 h	Network-limited
CSV to GeoParquet (433 tiles)	~ 8 – 12 h	I/O-limited
Tile index (433 tiles)	~ 5 min	16 workers, $1.55 \text{ files s}^{-1}$
TS classification	~ 24 – 48 h	32 joblib workers
DBSCAN clustering	~ 15 – 30 min	<code>n_jobs=-1</code> , ball tree
Sub-clustering	~ 2 – 4 h	32 workers, generator dispatch
Parquet write-back	~ 10 – 20 min	16 parallel writers
DuckDB viewport query (300 M pts)	30–80 ms	In-memory, CTE plan

722 B Installation and environment

```
723 conda create -n egms_tool python=3.12
724 conda activate egms_tool
725 conda install -c conda-forge pandas geopandas pyarrow duckdb \
726     scikit-learn scipy shapely tqdm pyqt6 flask flask-cors \
727     fiona gdal joblib
728 pip install alive-progress plotly kaleido concave-hull
729
730
```

```
731 # MKL-linked NumPy -- required on workstation for correct performance
732 conda install -c anaconda mkl numpy scikit-learn --force-reinstall
733
734 # EGMStoolkit (download step only)
735 git clone https://github.com/alexisInSAR/EGMStoolkit.git
736 echo PATH_TO/EGMStoolkit/src > \
737     $CONDA_PREFIX/Lib/site-packages/egmstoolkit.pth
738
```

739 **Windows only** (if ImportError: _ctypes):

```
740 copy ffi.dll %CONDA_PREFIX%\DLLs\ffi.dll
741 copy ffi.dll %CONDA_PREFIX%\DLLs\libffi-8.dll
742
```

744 B References

- 745 P. Berardino, G. Fornaro, R. Lanari, and E. Sansosti. A new algorithm for sur-
746 face deformation monitoring based on small baseline differential SAR interferograms.
747 *IEEE Transactions on Geoscience and Remote Sensing*, 40(11):2375–2383, 2002.
748 doi:[10.1109/TGRS.2002.803792](https://doi.org/10.1109/TGRS.2002.803792).
- 749 M. Berti, A. Corsini, S. Franceschini, and J. P. Iannacone. Automated classification of
750 persistent scatterers interferometry time series. *Natural Hazards and Earth System*
751 *Sciences*, 13(8):1945–1958, 2013. doi:[10.5194/nhess-13-1945-2013](https://doi.org/10.5194/nhess-13-1945-2013).
- 752 K. Bhuyan, K. Rana, J. V. Ferrer, F. Cotton, U. Ozturk, F. Catani, and N. Malik. Land-
753 slide topology uncovers failure movements. *Nature Communications*, 15:2633, 2024.
754 doi:[10.1038/s41467-024-46741-7](https://doi.org/10.1038/s41467-024-46741-7).
- 755 K. Bhuyan, K. Rana, U. Ozturk, L. Nava, A. Rosi, S. R. Meena, X. Fan, M. Floris,
756 C. Van Westen, and F. Catani. Towards automatic delineation of landslide source and
757 runout. *Engineering Geology*, 345:107866, 2025. doi:[10.1016/j.enggeo.2024.107866](https://doi.org/10.1016/j.enggeo.2024.107866).
- 758 F. Bovenga, J. Wasowski, D. Nitti, R. Nutricato, and M. Chiaradia. Using COS-
759 MO/SkyMed X-band and ENVISAT C-band SAR interferometry for landslides analysis.
760 *Remote Sensing of Environment*, 119:272–285, 2012. doi:[10.1016/j.rse.2011.12.013](https://doi.org/10.1016/j.rse.2011.12.013).
- 761 N. Casagli, W. Frodella, S. Morelli, V. Tofani, A. Ciampalini, E. Intrieri, F. Raspini,
762 G. Rossi, L. Tanteri, and P. Lu. Spaceborne, UAV and ground-based remote sensing
763 techniques for landslide mapping, monitoring and early warning. *Geoenvironmental*
764 *Disasters*, 4:9, 2017. doi:[10.1186/s40677-017-0073-1](https://doi.org/10.1186/s40677-017-0073-1).
- 765 N. Casagli, E. Intrieri, V. Tofani, G. Gigli, and F. Raspini. Landslide detection, monitoring
766 and prediction with remote-sensing techniques. *Nature Reviews Earth & Environment*,
767 4(1):51–64, 2023. doi:[10.1038/s43017-022-00373-x](https://doi.org/10.1038/s43017-022-00373-x).
- 768 F. Catani, P. Farina, S. Moretti, G. Nico, and T. Strozzi. On the applica-
769 tion of SAR interferometry to geomorphological studies: Estimation of land-
770 form attributes and mass movements. *Geomorphology*, 66(1–4):119–131, 2005.
771 doi:[10.1016/j.geomorph.2004.08.012](https://doi.org/10.1016/j.geomorph.2004.08.012).

- 772 F. Catani, V. Tofani, and D. Lagomarsino. Spatial patterns of landslide di-
773 mension: A tool for magnitude mapping. *Geomorphology*, 273:361–373, 2016.
774 doi:[10.1016/j.geomorph.2016.08.032](https://doi.org/10.1016/j.geomorph.2016.08.032).
- 775 N. Cenni, S. Fiaschi, and M. Fabris. Monitoring of land subsidence in the Po Plain
776 (Northern Italy) using GNSS and InSAR data. *Geomatics, Natural Hazards and Risk*,
777 12(1):2960–2987, 2021. doi:[10.1080/19475705.2021.1986317](https://doi.org/10.1080/19475705.2021.1986317).
- 778 X. Chen, P. Teatini, A. Rosi, F. Catani, and M. Floris. Spatiotemporal dynamics and
779 anomaly detection of land subsidence in delta areas: A case study from the Po river delta
780 using InSAR time series. *IEEE Journal of Selected Topics in Applied Earth Observations*
781 *and Remote Sensing*, 19:10381–10393, 2026. doi:[10.1109/JSTARS.2025.3650597](https://doi.org/10.1109/JSTARS.2025.3650597).
- 782 F. Cigna, C. Del Ventisette, V. Liguori, and N. Casagli. Advanced radar-interpretation
783 of InSAR time series for mapping and characterisation of geological processes. *Natural*
784 *Hazards and Earth System Sciences*, 11(3):865–881, 2011. doi:[10.5194/nhess-11-865-](https://doi.org/10.5194/nhess-11-865-2011)
785 [2011](https://doi.org/10.5194/nhess-11-865-2011).
- 786 C. Colesanti, A. Ferretti, F. Novali, C. Prati, and F. Rocca. SAR monitoring of
787 progressive and seasonal ground deformation using the permanent scatterers tech-
788 nique. *IEEE Transactions on Geoscience and Remote Sensing*, 41(7):1685–1701, 2003.
789 doi:[10.1109/TGRS.2003.813518](https://doi.org/10.1109/TGRS.2003.813518).
- 790 Copernicus Land Monitoring Service. European Ground Motion Service: Product User
791 Manual. Technical report, European Environment Agency, 2022. URL <https://land.copernicus.eu/en/technical-library/egms-product-user-manual>. Ac-
792 cessed: 2025.
- 793
- 794 M. Costantini, A. Ferretti, F. Minati, S. Falco, F. Trillo, D. Colombo, F. Novali, F. Mal-
795 varosa, C. Mammone, F. Vecchioli, A. Rucci, A. Fumagalli, J. Allievi, M. G. Ciminelli,
796 and S. Costabile. Analysis of surface deformations over the whole Italian territory by
797 interferometric processing of ERS, Envisat and COSMO-SkyMed radar data. *Remote*
798 *Sensing of Environment*, 202:250–275, 2017. doi:[10.1016/j.rse.2017.07.017](https://doi.org/10.1016/j.rse.2017.07.017).
- 799 M. Crosetto, L. Solari, M. Mróz, J. Balasis-Levinsen, N. Casagli, M. Frei, A. Oyen,
800 D. Moldestad, L. Bateson, L. Guerrieri, V. Commerci, and H. Andersen. The evolution
801 of wide-area DInSAR: From regional and national services to the European Ground
802 Motion Service. *Remote Sensing*, 12(12):2043, 2020. doi:[10.3390/rs12122043](https://doi.org/10.3390/rs12122043).
- 803 Y. Dong, L. Nava, R. Palamà, O. Monserrat, D. Festa, M. Floris, A. Rosi, and F. Catani.
804 Improving ground deformation classification by integrating InSAR time series with
805 geospatial information. *IEEE Transactions on Geoscience and Remote Sensing*, 63:
806 4709412, 2025. doi:[10.1109/TGRS.2025.3635271](https://doi.org/10.1109/TGRS.2025.3635271).
- 807 M. Ester, H.-P. Kriegel, J. Sander, and X. Xu. A density-based algorithm for discovering
808 clusters in large spatial databases with noise. In *Proceedings of the Second International*
809 *Conference on Knowledge Discovery and Data Mining (KDD-96)*, pages 226–231. AAAI
810 Press, 1996.

- 811 G. Farolfi, A. Piombino, and F. Catani. Fusion of GNSS and satellite radar inter-
812 ferometry: Determination of 3D fine-scale map of present-day surface displacements
813 in Italy as expressions of geodynamic processes. *Remote Sensing*, 11(4):394, 2019.
814 doi:[10.3390/rs11040394](https://doi.org/10.3390/rs11040394).
- 815 A. Ferretti, C. Prati, and F. Rocca. Permanent scatterers in SAR interferome-
816 try. *IEEE Transactions on Geoscience and Remote Sensing*, 39(1):8–20, 2001.
817 doi:[10.1109/36.898661](https://doi.org/10.1109/36.898661).
- 818 P. Fredi and E. Lupia Palmieri. *Il paesaggio fisico della Terra*. Zanichelli, Bologna, 2004.
- 819 E. Ghaderpour, P. Mazzanti, F. Bozzano, and G. S. Mugnozza. A fast and robust method
820 for detecting trend turning points in InSAR displacement time series. *Computers &
821 Geosciences*, 185:105546, 2024. doi:[10.1016/j.cageo.2024.105546](https://doi.org/10.1016/j.cageo.2024.105546).
- 822 A. Hooper. A multi-temporal InSAR method incorporating both persistent scatterer
823 and small baseline approaches. *Geophysical Research Letters*, 35(16):L16302, 2008.
824 doi:[10.1029/2008GL034654](https://doi.org/10.1029/2008GL034654).
- 825 A. Hooper, D. Bekaert, K. Spaans, and M. Arikan. Recent advances in SAR interferometry
826 time series analysis for measuring crustal deformation. *Tectonophysics*, 514–517:1–13,
827 2012. doi:[10.1016/j.tecto.2011.10.013](https://doi.org/10.1016/j.tecto.2011.10.013).
- 828 A. Hrysiwicz, K. Spaans, and A. Hooper. EGMStoolkit: a Python toolkit for down-
829 loading and processing European Ground Motion Service (EGMS) data. *Earth Science
830 Informatics*, 17:3117–3126, 2024. doi:[10.1007/s12145-024-01356-w](https://doi.org/10.1007/s12145-024-01356-w).
- 831 S. M. Mirmazloumi, Y. Wassie, J. A. Navarro, R. Palamà, V. Krishnakumar, A. Barra,
832 M. Crosetto, and O. Monserrat. Classification of ground deformation using Sentinel-1
833 persistent scatterer interferometry time series. *GIScience & Remote Sensing*, 59(1):
834 374–392, 2022. doi:[10.1080/15481603.2022.2030535](https://doi.org/10.1080/15481603.2022.2030535).
- 835 F. Raspini, S. Bianchini, A. Ciampalini, M. Del Soldato, R. Montalti, L. Solari, V. Tofani,
836 and N. Casagli. Continuous, semi-automatic monitoring of ground deformation using
837 Sentinel-1 satellites. *Scientific Reports*, 9:7253, 2019. doi:[10.1038/s41598-019-43884-8](https://doi.org/10.1038/s41598-019-43884-8).
- 838 P. Teatini, L. Tosi, T. Strozzi, L. Carbognin, U. Wegmüller, and F. Rizzetto. Mapping
839 regional land displacements in the Venice coastland by an integrated monitoring system.
840 *Remote Sensing of Environment*, 98(4):403–413, 2005. doi:[10.1016/j.rse.2005.08.002](https://doi.org/10.1016/j.rse.2005.08.002).
- 841 C. Werner, U. Wegmüller, T. Strozzi, and A. Wiesmann. GAMMA SAR and interferomet-
842 ric processing software. In *Proceedings of the ERS–Envisat Symposium*, Gothenburg,
843 Sweden, 2000. ESA SP-461.
- 844 Z. Yunjun, H. Fattahi, and F. Amelung. Small baseline InSAR time series analysis: un-
845 wrapping error correction and noise reduction. *Computers & Geosciences*, 133:104331,
846 2019. doi:[10.1016/j.cageo.2019.104331](https://doi.org/10.1016/j.cageo.2019.104331).
- 847 H. A. Zebker, P. A. Rosen, and S. Hensley. Atmospheric effects in interferometric synthetic
848 aperture radar surface deformation and topographic maps. *Journal of Geophysical
849 Research: Solid Earth*, 102(B4):7547–7563, 1997. doi:[10.1029/96JB03804](https://doi.org/10.1029/96JB03804).